



Global seismological shear velocity and attenuation: A comparison with experimental observations

Colleen A. Dalton^{a,*}, Göran Ekström^b, Adam M. Dziewonski^a

^a Department of Earth and Planetary Sciences, Harvard University, 20 Oxford Street, Cambridge, MA 02138, USA

^b Lamont-Doherty Earth Observatory, Columbia University, 61 Route 9W, Palisades, NY 10964 USA

ARTICLE INFO

Article history:

Received 1 July 2008

Received in revised form 23 March 2009

Accepted 9 April 2009

Available online 19 May 2009

Editor: L. Stixrude

Keywords:

seismology

attenuation

ABSTRACT

We present a comparison of seismologically observed shear velocity and attenuation on a global scale. These observations are also compared with laboratory measurements of the same quantities made on fine-grained olivine and extrapolated to upper-mantle conditions. The analysis is motivated by recent developments in global attenuation tomography and in laboratory measurements of velocity and attenuation at seismic frequencies and upper-mantle temperatures. The new attenuation model QRFSI12 is found to be strongly anti-correlated with global velocity models throughout the upper mantle, and individual tectonic regions are each characterized by a distinct range of attenuation and velocity values in the shallow upper mantle. Overall, lateral temperature variations can explain much of the observed variability in velocity and attenuation. The seismological velocity–attenuation relationship for oceanic regions agrees with the experimental observations at depths >100 km and indicates lateral temperature variations of 150°–200 °C at 150 and 200 km beneath the seafloor. The seismic properties of cratonic regions deviate from the experimental trends at depths <250 km, suggesting differences between oceanic and cratonic composition or water content at these depths. Globally, seismic properties shift into better agreement with the mineral-physics data at depths of ~125 km and ~225 km beneath oceans and cratons, respectively, which may indicate the base of a compositional boundary layer.

© 2009 Elsevier B.V. All rights reserved.

1. Introduction

Inferring the physical and chemical state of the Earth's interior is a primary application of seismological models. Numerous studies have proposed interpretations of seismic velocity models in terms of temperature (e.g., Humler et al., 1993; Ritzwoller et al., 2004; Priestley and McKenzie, 2006), composition (e.g., Trampert et al., 2004), and the presence of melt (e.g., Anderson and Sammis, 1970; Dunn and Forsyth, 2003) or water (Gaherty et al., 1999). It has also been pointed out that grain size (Jackson et al., 2002), anisotropy (Ekström and Dziewonski, 1998), and mineral phase transformations (Stixrude and Lithgow-Bertelloni, 2007) can further complicate the interpretation of such models. Two approaches help to overcome the issue of non-unique interpretation. One, researchers have considered other geophysical observables in addition to shear-wave velocity, including bulk-sound speed (e.g., Su and Dziewonski, 1997), density (e.g., Ishii and Tromp, 1999), heat flow (e.g., Shapiro and Ritzwoller, 2004), electrical conductivity (e.g., Evans et al., 2005), and mantle xenoliths (e.g., James et al., 2004). Two, laboratory measurements of the density and elastic properties of numerous natural and synthetic mineral and

rock samples have facilitated a more quantitative interpretation of seismic velocity (e.g., Goes et al., 2000; Lee, 2003; Stixrude and Lithgow-Bertelloni, 2005; Faul and Jackson, 2005).

Jointly interpreting models of seismic velocity and attenuation (Q^{-1}) is a potentially powerful approach for constraining the state of the mantle, as attenuation is influenced differently by various mantle properties than velocity is. The differences are illustrated schematically in Fig. 1. The strong temperature sensitivity of attenuation is well documented and has been observed in the laboratory: $Q^{-1} \propto \exp(-E/RT)$, where T is temperature, E is activation energy, and R is the gas constant (Anderson, 1967). Increasing temperature leads to higher attenuation and slower shear velocity, resulting in the trends displayed in Fig. 1. Attenuation is expected to be much less sensitive to major-element compositional variations than velocity is (red curve in Fig. 1). Limited experimental data support the idea of minimal compositional sensitivity; moreover, attenuation is independent of the anharmonic shear modulus, which is influenced by compositional variations (Faul and Jackson, 2005). Partial melt has been shown to reduce velocities and increase attenuation, although the details of this effect depend on the mechanism (green curves in Fig. 1). Finally, it is expected that water, which is incorporated in anhydrous minerals as hydrogen-related point defects, will strongly enhance attenuation and influence velocity only indirectly through anelastic dispersion (blue curve in Fig. 1; Karato and Jung, 1998; Karato, 2003). This relation has not yet been studied

* Corresponding author. Now at Department of Earth Sciences, Boston University.
E-mail address: dalton@bu.edu (C.A. Dalton).

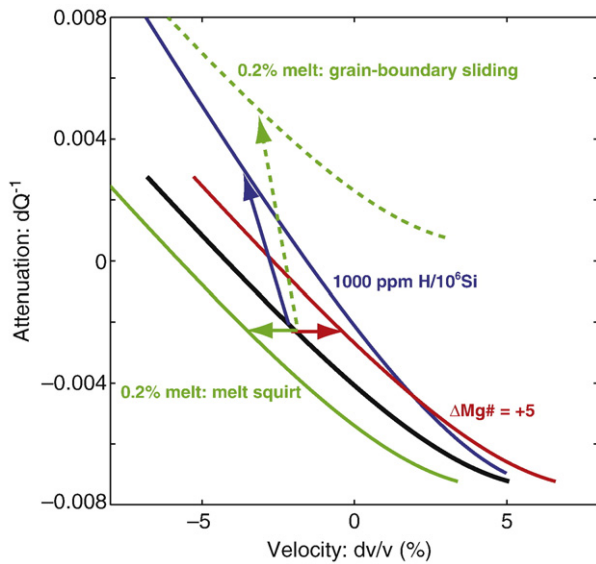


Fig. 1. Schematic illustration of the expected relationship between shear velocity and attenuation due to lateral temperature variations at 150-km depth. The black curve represents the expected trend for dry, melt-free olivine, given a temperature range of 400°–1400 °C. An increase in Mg# by five units (e.g., from 88 to 93; red) results in a uniform velocity increase of 0.07 km/s (Lee, 2003), and it is assumed that attenuation is not affected. The effect of 0.2% melt on the velocity–attenuation curve is predicted assuming a melt-squirt mechanism (solid green; Hammond and Humphreys, 2000a,b) and as inferred from experimental grain-boundary sliding data (dashed green; Jackson et al., 2004; Faul et al., 2004). The influence of increasing water content from 0 to 1000 H/10⁶ Si (blue) derives from Karato (2003), Yang et al. (2007), and Harmon et al. (2009). (For interpretation of the references to colour in this figure legend, the reader is referred to the web version of this article.)

rigorously in the laboratory but is inferred through experiments on the role of water on diffusion creep, dislocation creep, and grain-boundary mobility.

It is clear from Fig. 1 that the effect of lateral temperature variations on the velocity–attenuation relationship can depend on the composition and water content of mantle rocks and on if and how much partial melt is present. Certain factors, such as major-element composition and melt squirt, affect only one variable and not the other, thereby shifting the thermal trend from left to right (or up and down). Other factors, such as water content and melt-enhanced grain-boundary sliding, affect both variables, and the effect may be temperature dependent, thereby altering the slope of the thermal trend. These three pieces of information – the magnitude of attenuation and velocity and the nature of their relationship – may help to distinguish between compositional, melt-related, and water-related effects on seismic observations.

There have been relatively few efforts to interpret jointly seismologically observed attenuation and velocity in terms of temperature, composition, and other factors. Romanowicz (1990) observed a strong spherical-harmonic degree-2 pattern in global Rayleigh wave attenuation at ~200-s period and inferred a thermal origin for this feature based on agreement with the degree-2 signal in shear velocity models in the same depth range. In a series of papers, Romanowicz and co-workers have interpreted agreement between the patterns of high attenuation in the transition zone, the locations of hotspots, and the two low-velocity “superplume” anomalies at the base of the mantle as evidence of coherent upwelling flow between the lower and upper mantle (Romanowicz, 1994, 1995; Romanowicz and Gung, 2002; Gung and Romanowicz, 2004). Billien et al. (2000) reported qualitative agreement between global patterns of Rayleigh wave attenuation and velocity for periods <80 s and inferred that a large amount of attenuation must occur in the lithosphere. By comparing the velocity and attenuation models of Billien et al. (2000) with temperature estimates for the continental upper mantle,

Artemieva et al. (2004) found only weak correlation. Roth et al. (2000) compared images of P-wave velocity and attenuation for the Tonga/Fiji subduction zone and derived an empirical relationship between the two quantities that was generally consistent with the available laboratory observations. Lawrence et al. (2006) mapped P- and S-wave travel-time and attenuation residuals throughout North America. They interpreted the high attenuation and slow velocities in western North America in terms of high temperature and possibly elevated water content and the fast velocities and moderate attenuation within the cratonic upper mantle in terms of chemical alteration.

Explanations for the lateral variations in velocity and attenuation throughout the upper mantle may help to address two key issues in particular: the origin of the upper-mantle low-velocity zone (~80–220-km depth) and the role of compositional heterogeneity within the continental lithosphere. The low-velocity zone (LVZ) appears to be ubiquitous beneath the oceans and is characterized by (1) slower velocity (e.g., Nishimura and Forsyth, 1989), (2) higher attenuation (e.g., Durek and Ekström, 1996), and (3) higher electrical conductivity (Lizarralde et al., 1995; Evans et al., 1999) than the mantle located above and below it. The LVZ has been attributed to the presence of partial melt (Anderson and Sammis, 1970; Mierdel et al., 2007), or to elevated water content (Hirth and Kohlstedt, 1996; Karato and Jung, 1998), or to solid-state thermal mechanisms (Faul and Jackson, 2005; Stixrude and Lithgow-Bertelloni, 2005). New constraints on the seismic properties of this region will hopefully reduce the number of possible explanations.

Jordan (1979) proposed that the negative thermal buoyancy in cold continental roots is balanced by positive compositional buoyancy, and he suggested that removal of basaltic magma from the rocks that now comprise the continental lithosphere created a residuum characterized by lower density and faster shear-wave speeds than asthenospheric mantle at the same depth and temperature. Recent efforts to update this work both support (Lee, 2003) and dispute (Schutt and Leshner, 2006) a role for compositional heterogeneity in controlling shear-wave velocities beneath continents, and resolution of this discrepancy has implications for estimates of temperature and viscosity in the continental lithosphere.

Recent laboratory measurements of shear modulus and attenuation in olivine, made at seismic frequencies and high temperatures, constrain the effect of anelasticity on seismic velocity as well as the temperature dependence of attenuation in the relevant frequency band (e.g., Gribb and Cooper, 1998; Jackson et al., 2002), and several studies have utilized these data for interpreting regional seismic models. Faul and Jackson (2005) used these results to infer that a low-velocity, high-attenuation zone beneath oceanic lithosphere could be achieved by temperature alone, and that fast velocities beneath the Yilgarn craton in western Australia can be explained by cold temperatures. Yang et al. (2007) utilized the laboratory data to argue that vertical profiles of attenuation and velocity beneath young seafloor in the Pacific were not simultaneously consistent with thermal effects alone, and they suggested that partial melt must be present to at least 100-km depth in these regions to explain their observations. Priestley and McKenzie (2006) have argued that the temperature dependence of velocity determined by Faul and Jackson's fit to the experimental data is inconsistent with a comparison of oceanic thermal models and seismologically observed velocity.

In this study, we present a comparison of seismological observations and experimental measurements of shear-wave velocity and attenuation on a global scale. In particular, we take advantage of recent experimental observations of shear velocity and attenuation in olivine (Faul and Jackson, 2005) and our new, global, three-dimensional model of shear attenuation in the upper mantle. This model, QRFSI12, is derived from large datasets of surface-wave amplitudes, and we account for source, instrument, and focusing effects on the amplitude data. The development of QRFSI12 and tests to quantify the robustness of the model are described in a separate paper (Dalton et al., 2008; hereinafter DED08).

We show that QRFSI12 is strongly anti-correlated with global shear velocity models in the upper mantle, and comparison of attenuation and velocity models reveals distinct regional trends in the relationship between the two quantities. Seafloor age-dependent differences in the velocity–attenuation relationship for oceans are small at depths >150 km, although continental areas of recent orogeny remain seismically distinct from Precambrian platforms and shields at greater depths. The experimentally based model of [Faul and Jackson \(2005\)](#) is compared to the seismological models, with an emphasis on understanding the ability of lateral temperature variations to explain the seismic observations on a global scale. We find that in oceanic regions, the seismic models agree well with the experimental trends at depths >100 km, and the temperature range beneath oceans inferred from the seismic models is ~ 200 °C at 150- and 200-km depth. Beneath old-continental regions, the seismic observations deviate from the mineral-physics predictions at depths <250 km. We suggest that differences in the major-element composition or water content of oceanic and continental upper mantle in the depth range 150–250 km are consistent with the observations and may also be related to the base of the lithosphere.

2. Seismological shear attenuation and velocity

QRFSI12 is a spherical-harmonic degree-12 model of shear attenuation in the upper mantle. It was derived from fundamental-mode Rayleigh wave amplitude measurements in the period range 50–250 s; between 30,000 and 50,000 amplitudes were included at each period. More so than the travel-time and phase-delay measurements from which seismic velocity models are derived, surface-wave amplitudes require a complex interpretation. Factors other than attenuation influence the amplitude, including uncertainty in the knowledge of source excitation and instrument response as well as focusing and defocusing by lateral velocity heterogeneity. Developing methods to remove these extraneous effects has been the objective of several earlier surface-wave attenuation studies (e.g., [Romanowicz, 1990](#); [Selby and Woodhouse, 2000](#)). Our approach to this problem is

to invert the amplitude data set simultaneously for the coefficients of the attenuation model as well as for terms that correspond to each of the other factors: frequency-dependent amplitude correction factors for each earthquake and each station, and Rayleigh wave phase-velocity maps to account for focusing effects. The phase-velocity maps are constrained by both phase-delay and amplitude measurements, and we have shown how focusing effects can map into inaccurate attenuation structure if not accounted for ([Dalton and Ekström, 2006](#)).

The details of QRFSI12 are described in DED08. The robust features include a strong correlation with surface tectonics for depths shallower than 200 km, and, at greater depths, zones of high attenuation located in the southeastern Pacific and eastern Africa, with low attenuation beneath a number of subduction zones in the western Pacific ([Fig. 2](#)). One of the most striking characteristics of QRFSI12 is the strong anti-correlation with global shear velocity models, particularly in the shallow mantle ([Figs. 2 and 3](#)). This correlation is present in comparisons performed using a number of global velocity models ([Fig. 3a](#)) and is much weaker when earlier global attenuation models are instead compared to the velocity models ([Fig. 3b](#)).

In [Fig. 4a](#), it is clear that individual tectonic regions are each characterized by a well-defined range of attenuation and velocity values at 100-km depth. We have sampled QRFSI12 and shear velocity model S362ANI ([Kustowski et al., 2008](#)) at 5762 points evenly spaced across the globe, and we classify each of these points by tectonic region (GTR1; [Jordan, 1981](#)). For this analysis, exposed Precambrian shields and platforms are grouped together with platforms overlain by undisturbed Phanerozoic cover (“old continents”). To determine the contours, the area shown in [Fig. 4a](#) is divided into small grid cells, and the contours connect cells with a similar point density. Each grid cell spans 0.025 km/s in velocity and 0.00125 units in attenuation. Young, intermediate-age, and old oceanic regions separate from one another in velocity–attenuation space ([Fig. 4a](#)), with young oceans characterized by some of the slowest velocity and highest attenuation values observed. The continental regions can be split into two groups. Higher attenuation and slower velocity characterize regions of recent or active orogeny and magmatism, whereas very low attenuation and

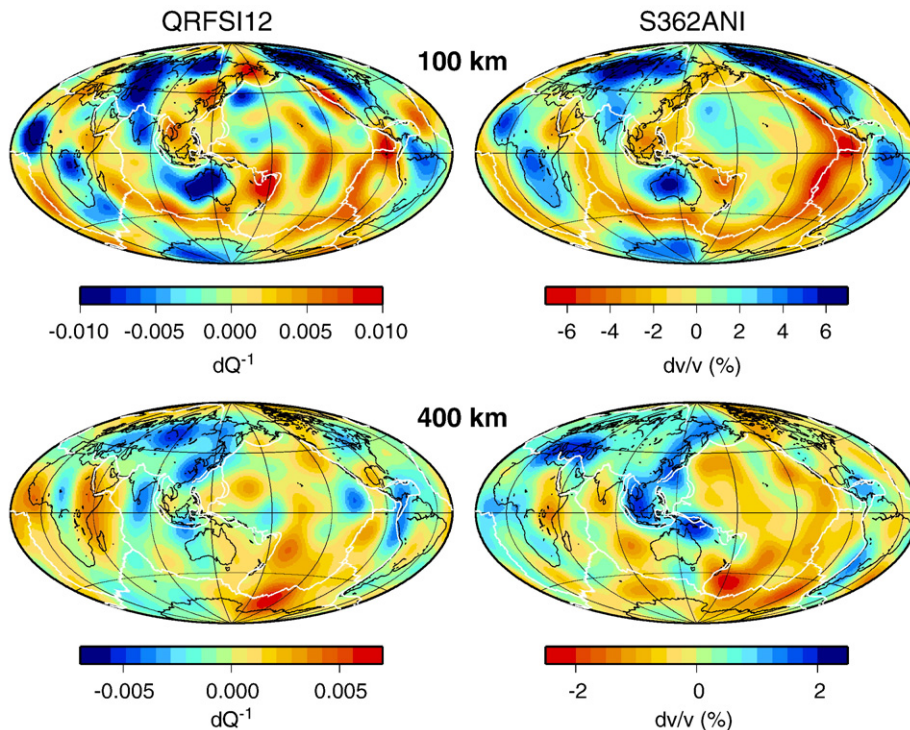


Fig. 2. Comparison of global shear attenuation (left) and shear velocity (right) models at 100-km and 400-km depth. The attenuation model QRFSI12 is plotted as the deviation away from the globally averaged Q_{μ}^{-1} value at each depth. Isotropic velocity from model S362ANI ([Kustowski et al., 2008](#)) is shown here expanded in spherical harmonics up to degree 12.

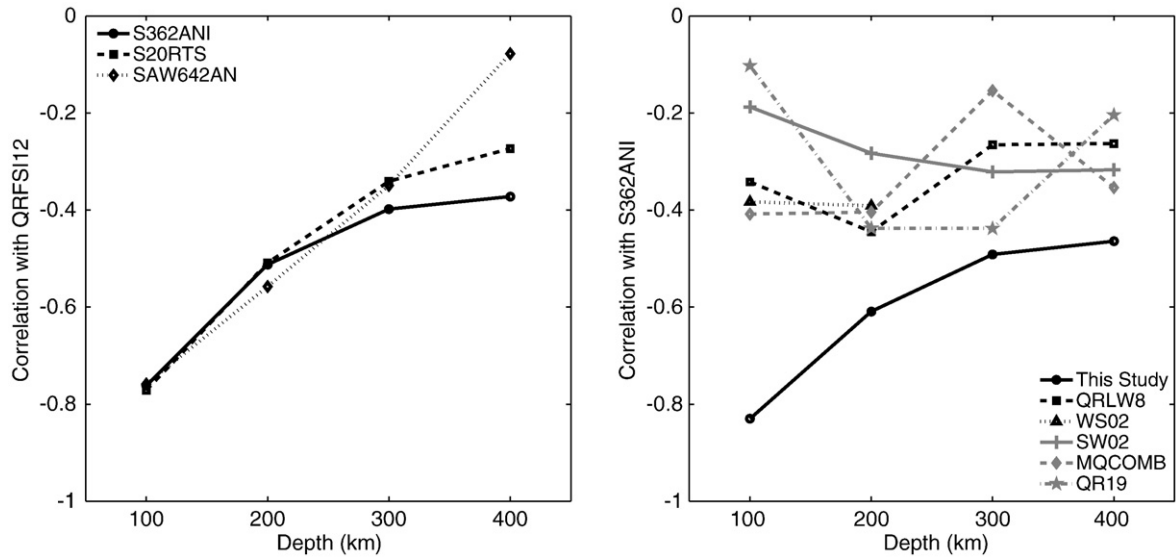


Fig. 3. (Left) Correlation coefficient as a function of depth between QRFSI12 and three shear velocity models: S362ANI, S20RTS (Ritsema et al., 1999), and SAW642AN (Panning and Romanowicz, 2006). Correlation is calculated using spherical-harmonic degrees 1–12. (Right) Correlation as a function of depth between S362ANI and six shear attenuation models: QRFSI12, QRLW8 (Gung and Romanowicz, 2004), WS02 (Warren and Shearer, 2002), SW02 (Selby and Woodhouse, 2002), MQCOMB (Reid et al., 2001), and QR19 (Romanowicz, 1995). Correlation is calculated using degrees 1–8. Model WS02 is only defined for depths <220 km.

fast velocity are associated with undisturbed shields and platforms. These same features are present if a different global velocity model is instead used for the comparison, such as SAW642AN (Panning and Romanowicz, 2006) or S20RTS (Ritsema et al., 1999).

The correlation coefficient that defines the strength of the linear relationship between velocity and attenuation varies between the five regions considered. At 100-km depth, it is strongest for the continental regions (correlation equals -0.79 for old shields and platforms and -0.72 for orogenic areas) and somewhat weaker for the oceans (-0.63 , -0.56 , and -0.44 for old, intermediate-age, and young oceans, respectively). In the GTR1 parameterization, young oceans include some tectonically complex areas, like back-arc spreading centers, that may complicate the relationship between velocity and

attenuation. At a depth of 150 km, the two continental regions still separate into two distinct groups; however, the three oceanic regions exhibit considerably more overlap than at 100 km, most likely because little, if any, oceanic lithosphere extends to 150-km depth (Fig. 4b).

3. Comparison with experimental measurements

The influence of temperature on the elastic and anelastic properties of olivine and other upper-mantle minerals has been measured in the laboratory (e.g., Duffy and Anderson, 1989; Gribb and Cooper, 1998; Jackson et al., 2002), and in general the sign of the temperature derivatives is as expected: negative for modulus and velocity, and positive for attenuation. The majority of experimental data for modulus

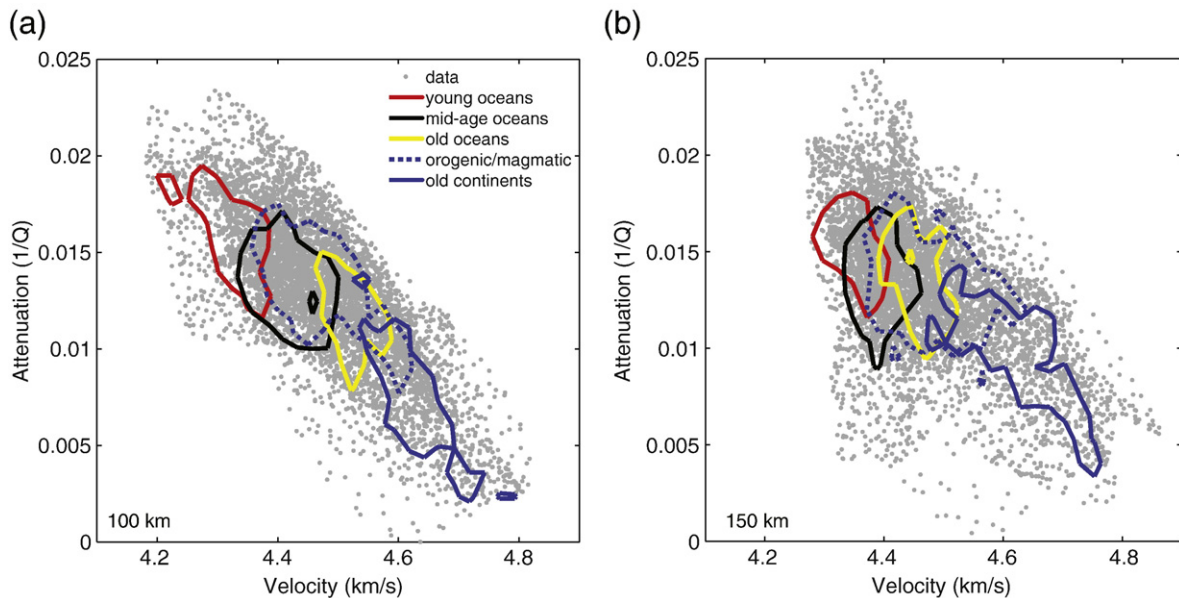


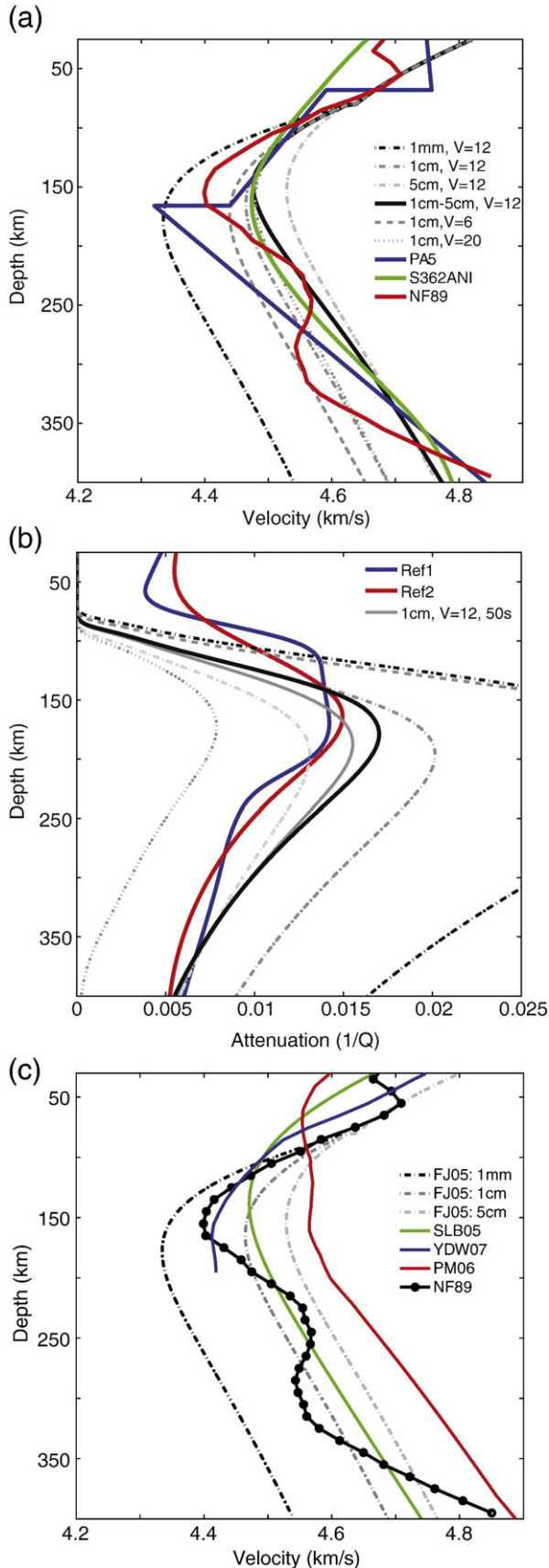
Fig. 4. Scatter plot showing the shear velocity (S362ANI) and shear attenuation (QRFSI12) values at (a) 100-km depth and (b) 150-km depth, sampled at 5762 evenly spaced points. Model S362ANI is truncated at spherical-harmonic degree 12, and isotropic (Voigt average) velocity values are used. Contours enclose 50% of the points from each of the GTR1 tectonic regions. Red: young oceanic regions <25 m.y. (778 points). Black: intermediate-age oceanic regions 25–100 m.y. (1994 points). Yellow: old oceanic regions >100 m.y. (743 points). Dashed blue: Phanerozoic orogenic zones and magmatic belts (1256 points). Solid blue: Precambrian shields and platforms, and Phanerozoic platforms (991 points). (For interpretation of the references to colour in this figure legend, the reader is referred to the web version of this article.)

and velocity have been collected at frequencies well above the seismic band ($\sim 10^6$ Hz versus 10^{-3} to 10^0 Hz), and thus historically it has been necessary to estimate the relaxed modulus and velocity at high

Table 1
Parameter values used for calculations.

| Parameter | Value |
|------------|---|
| κ | 10^{-6} m ² /s |
| T_P | 1623 K |
| α_T | 2.9×10^{-5} K ⁻¹ |
| c_p | 1350 J kg ⁻¹ K ⁻¹ |
| β | 6.0×10^{-12} Pa ⁻¹ |
| ρ_0 | 3310 kg m ⁻³ |

These values are assumed to be representative of the upper mantle and are from Turcotte and Schubert (1982) and Faul and Jackson (2005).



temperature and low frequencies by correcting for the effects of an assumed attenuation model (e.g., Liu et al., 1976). Furthermore, seismic evidence suggests that attenuation in the mantle is frequency dependent, at least in some bands (Sipkin and Jordan, 1979), and thus it is not clear how to relate measurements of attenuation made at ultrasonic frequencies (Sato et al., 1988) to seismic-wave propagation in the Earth. Recent experimental data obtained at high temperature (1200°–1300 °C) and low frequency (10^{-3} to 10^0 Hz) constrain the temperature, frequency, and grain-size dependence of shear attenuation and modulus simultaneously: increasing temperature, decreasing grain size, and increasing period all lead to lower modulus and higher attenuation (Gribb and Cooper, 1998; Jackson et al., 2002). The new observations underscore the enhanced temperature sensitivity of shear velocity at low frequencies and high temperatures and provide quantitative laboratory observations of seismic attenuation in the relevant frequency band.

Faul and Jackson (2005) derived a model, by fitting the experimental data of Tan et al. (2001) and Jackson et al. (2002), that describes the temperature, frequency, and grain-size dependence of the shear modulus and shear attenuation. Their model is based on the Burgers rheological body, with modifications to include a distribution of anelastic relaxation times, grain-size dependence, and temperature dependence. The model allows extrapolation to upper-mantle conditions, which is valuable since the experiments were performed on fine-grained olivine (grain size = 3–165 μ m) at relatively low pressure (<300 MPa). In the following sections, we compare the experimental data with the seismologically observed velocity and attenuation; comparison with oceanic profiles from global seismic models has not been shown before. We also present the first application of the mineral-physics model to laterally varying global seismic structure.

3.1. Vertical profiles

Fig. 5a and b compare observed vertical seismic profiles with profiles predicted using the model of Faul and Jackson (2005). All profiles are approximately representative of 100-Myr seafloor. For the predictions, a geotherm is calculated using a half-space cooling model, a potential temperature of 1350 °C, and values of thermal diffusivity (κ), the coefficient of thermal expansion (α_T), and specific heat (c_p) as specified in Table 1. Pressure and density are calculated assuming

Fig. 5. Comparison of observed and predicted shear-wave velocity (a) and attenuation (b) profiles. The predictions are representative of old (100-Myr) oceanic lithosphere, and the dot-dash grey lines indicate grain-size values of 1 mm, 1 cm, and 5 cm, assuming an activation volume $V = 12 \times 10^{-6}$ m³/mol. Thick black line represents an assumption of increasing grain size with depth. The influence of a smaller ($V = 6 \times 10^{-6}$ m³/mol) and larger ($V = 20 \times 10^{-6}$ m³/mol) activation volume, for a grain size of 1 cm, is indicated by dashed and dotted grey lines. (a) All velocity profiles plotted at frequency of 1 Hz. (b) Predicted profiles calculated using the period–depth relationship described in the text. Colored profiles correspond to versions of QRFS12 constructed with two different reference models. Solid grey line indicates assumption of a constant period of 50 s for 1-cm grain size. (c) Comparison of several velocity predictions; models are described in the text and plotted at 1 Hz. NF89 results are shown for reference.

values of adiabatic compressibility (β) and zero-pressure density (ρ_0) as given in Table 1.

The predicted profiles of shear velocity in Fig. 5a are calculated using an activation volume $V = 12 \times 10^{-6} \text{ m}^3/\text{mol}$, a period of 1 s, and a range of grain-size values ($d = 1 \text{ mm}$, 1 cm, 5 cm). These curves are compared to seismologically observed profiles of isotropic shear velocity. Model PA5 (Gaherty et al., 1996) was determined for the corridor connecting Tonga and Hawaii and represents Pacific upper mantle beneath old seafloor (100–125 Myr). As PA5 is defined at a reference frequency of 35 mHz, we use the attenuation structure determined for this corridor by Gaherty et al. (1996) to obtain a version of PA5 at 1 Hz, using the dispersion relation (Liu et al., 1976)

$$v(\omega_2) \approx v(\omega_1) \left[1 + \frac{1}{\pi Q} \ln \left(\frac{\omega_2}{\omega_1} \right) \right], \quad (1)$$

where ω_2 and ω_1 indicate the angular frequencies of interest. Model S362ANI (Kustowski et al., 2008) is a global mantle model of radially anisotropic shear-wave velocity. The profile shown in Fig. 5a represents a global average beneath old oceanic lithosphere ($>100 \text{ Myr}$) and is plotted at 1 Hz. The shear velocity model of Nishimura and Forsyth (1989), here abbreviated NF89, is representative of Pacific upper mantle corresponding to seafloor ages $>110 \text{ Myr}$; isotropic velocities are shown. Nishimura and Forsyth neglected anelastic dispersion in the development of their preferred model but performed tests to investigate how considering attenuation would alter their model. We use the results of their tests to correct, in an approximate way, their preferred model to 1 Hz.

The two observed attenuation profiles in Fig. 5b were obtained in the development of model QRFSI12 and represent a global average beneath seafloor older than 100 Myr. The profiles correspond to two different starting models, one with strong gradients above and below the low- Q_μ zone between 80 and 220 km (Ref 1), the other constant at $Q_\mu = 146$ throughout the upper mantle (Ref 2). Both profiles contain the same first-order features: a significant increase to high attenuation at $\sim 100 \text{ km}$, a sharp decrease to much weaker attenuation at $\sim 200\text{--}250 \text{ km}$, and a steady decrease in attenuation down to 450 km. The maximum attenuation occurs in the depth range 125–175 km. Frequency-dependent attenuation ($Q^{-1} \propto \omega^{-0.26}$) is inherent in the model of Faul and Jackson (2005), and thus for the model predictions, it is necessary to choose a frequency that is consistent with QRFSI12. We do not account for possible frequency-dependent attenuation in the construction of QRFSI12, and thus at each depth, QRFSI12 is primarily constrained by the Rayleigh wave frequency most sensitive to that depth (e.g., that Q at 100-km depth is relevant to 75-s waves and at 350 km to 250-s waves). We therefore choose a different period for the model prediction at each depth, using the relationship: period = $3 \times \text{depth(m)}/4200$ (Forsyth, 1992) to approximate the depth sensitivity of Rayleigh waves of a certain period. Implications of this treatment of frequency dependence are discussed below.

In Fig. 5a, it is apparent that a grain size of 1 mm predicts velocities that are slower than observed at all depths $>100 \text{ km}$, that a grain size of 5 cm predicts faster velocities than observed in the depth range 100–300 km, and that with $d = 1 \text{ cm}$, the predicted and observed velocities agree well in the depth range 100–150 km. Faul and Jackson (2005) showed that one way to match simultaneously the magnitude of the low-velocity zone at $\sim 150 \text{ km}$ and the steep velocity gradient at greater depth is to allow grain size to increase with depth. The solid black line in Fig. 5a represents a prediction for which grain size increases linearly from 1 cm at depths $<140 \text{ km}$ to 5 cm at 400-km depth; this curve reproduces the major features of the seismological models for depths $>75 \text{ km}$. We note that Faul and Jackson (2005) previously observed that their mineral-physics model cannot match the constant-velocity lid (depth $<60 \text{ km}$) contained in the observed velocity profiles.

The predictions of vertical attenuation profiles (Fig. 5b) are more strongly sensitive to assumed grain size and activation volume, and clearly $d = 1 \text{ mm}$ predicts attenuation that is much too high, while $d = 5 \text{ cm}$ predicts lower-than-observed attenuation for depths $<200 \text{ km}$. Allowing grain size to increase over the depth range 140–400 km yields an attenuation profile that matches reasonably well the high-attenuation zone at 150–200 km in addition to the steep negative gradient at greater depth. The mineral-physics model prescribes purely elastic behavior for temperatures $<950 \text{ }^\circ\text{C}$, and thus the observed and predicted attenuation profiles differ for depths $<75 \text{ km}$.

Tradeoffs exist between grain size and activation volume. They are slight for velocity; Fig. 5a compares velocity predictions for $d = 1 \text{ cm}$ and $V = 6, 12, \text{ and } 20 \times 10^{-6} \text{ m}^3/\text{mol}$. The tradeoffs are more significant for attenuation; $d = 1 \text{ mm}$ and $V = 12 \times 10^{-6} \text{ m}^3/\text{mol}$ yields a similar profile as $d = 1 \text{ cm}$ and $V = 6 \times 10^{-6} \text{ m}^3/\text{mol}$ (Fig. 5b). However, the need to match simultaneously the observed velocity and attenuation profiles constrains the range of allowable parameters. For example, $d = 1 \text{ mm}$ and $V = 20 \times 10^{-6} \text{ m}^3/\text{mol}$ predicts a reasonable attenuation profile for depths $<250 \text{ km}$ but velocities that are too slow (not shown).

The model of Faul and Jackson (2005; FJ05) is one of several recent efforts to determine expressions for shear velocity in terms of relevant parameters; Fig. 5c compares four such predictive models at 1 Hz. Stixrude and Lithgow-Bertelloni (2005; SLB05) calculated the equilibrium phase assemblage and the resulting physical properties along an oceanic upper-mantle geotherm; their Eq. (7) is plotted in Fig. 5c. The model of Yang et al. (2007; YDW07) is based on the authors' empirical fit to their seismological velocity and attenuation models for Pacific upper mantle. In this model, attenuation is tripled over the depth range 50–80 km to produce the effect of increasing water content with depth, and velocity is thus indirectly affected. The model of Priestley and McKenzie (2006; PM06) resulted from a comparison of oceanic thermal models and observed SV wave speeds in the Pacific. Both PM06 and YDW07 are corrected for anelastic dispersion using the values applied to NF89 in Fig. 5a. FJ05, SLB05, and YDW07 yield similar predictions in the range 100–200 km, and at greater depth the velocity gradient for these models is shallower than the observations, as in Fig. 5a. At all depths $>100 \text{ km}$, PM06 predicts faster-than-observed velocities, an issue that would be more pronounced if isotropic velocities were shown, since $V_{SH} > V_{SV}$ in the oceanic uppermost mantle.

In summary, our results agree with Faul and Jackson (2005): using temperature profiles and values of grain size and activation volume that are appropriate for 100-Myr oceanic upper mantle, the mineral-physics model can match the seismologically observed velocity and attenuation profiles. The implication of this result for the physical state of the upper mantle is that it is possible to produce a low-velocity/high-attenuation zone in the oceanic upper mantle, away from the mid-ocean ridge, without invoking the presence of partial melt or water. This result is further supported by the good fit to velocity observations provided by SLB05, which is also based on solid-state considerations; there are no other experimentally based models for attenuation with which to compare. However, it is not possible to entirely rule out melt or water, since exact values for upper-mantle grain size and activation volume are not known and since the effects of melt and water on velocity and attenuation are not fully understood.

Uncertainties in the attenuation model are likely larger than in the various velocity models, and thus some mismatch between predicted and observed attenuation profiles is expected, whereas the observed wave speeds in Fig. 5a are more tightly constrained. Furthermore, it is unclear how best to treat the frequency dependence of attenuation. Sipkin and Jordan (1979) suggested an increase in Q_{scs} with frequency in the range 0.1–2.5 Hz, and frequency dependence of attenuation is one of the most robust results obtained from laboratory measurements (e.g., Jackson et al., 2002). However, strong seismological

evidence for or against such frequency dependence is lacking in the band of our interest, 0.004–0.02 Hz. For comparison, Fig. 5b shows a vertical attenuation profile calculated for $d = 1$ cm, $V = 12 \times 10^{-6}$ m³/mol, and a constant period of 50 s. Compared to the equivalent prediction made assuming the frequency–depth relationship described above, this profile exhibits slightly lower attenuation for depths >100 km but overall does not affect our conclusions.

3.2. Laterally varying velocity and attenuation

The lateral variations in seismologically observed velocity and attenuation show regional trends that vary with depth. In Fig. 6, the global attenuation (QRFSI12) and velocity (S362ANI) models have both been expanded to spherical-harmonic degree 12 so that they have the same spatial resolution, and the models are then sampled at 5762 evenly spaced points. To emphasize the regional trends, contours that enclose 75% of the points from each of three tectonic regions are

also plotted: old continents (described in section 2), oceans younger than 70 Myr, and oceans older than 70 Myr. The contours are constructed as described in section 2. This division of the seafloor is consistent with the observed flattening of the seafloor depth–age curve globally (e.g., Stein and Stein, 1992) and the proposed reheating of central Pacific lithosphere older than 70 Myr (Ritzwoller et al., 2004).

The best-fitting lines through each set of points have been determined by orthogonal regression. The correlation coefficient and the slope dQ^{-1}/dV_S of the best-fitting lines are reported for each set of points in Table 2. The correlation coefficients are all significant at >90% confidence, and most are significant at >95% confidence. The 95%-confidence bounds on the best-fitting lines have been determined by *t*-test statistics and are reported in Table 2 and Fig. 7 (dashed lines). Although sampling the global velocity and attenuation models at nearly 6000 locations allows thorough global coverage, the spherical-harmonic degree-12 expansion of the models results in many fewer

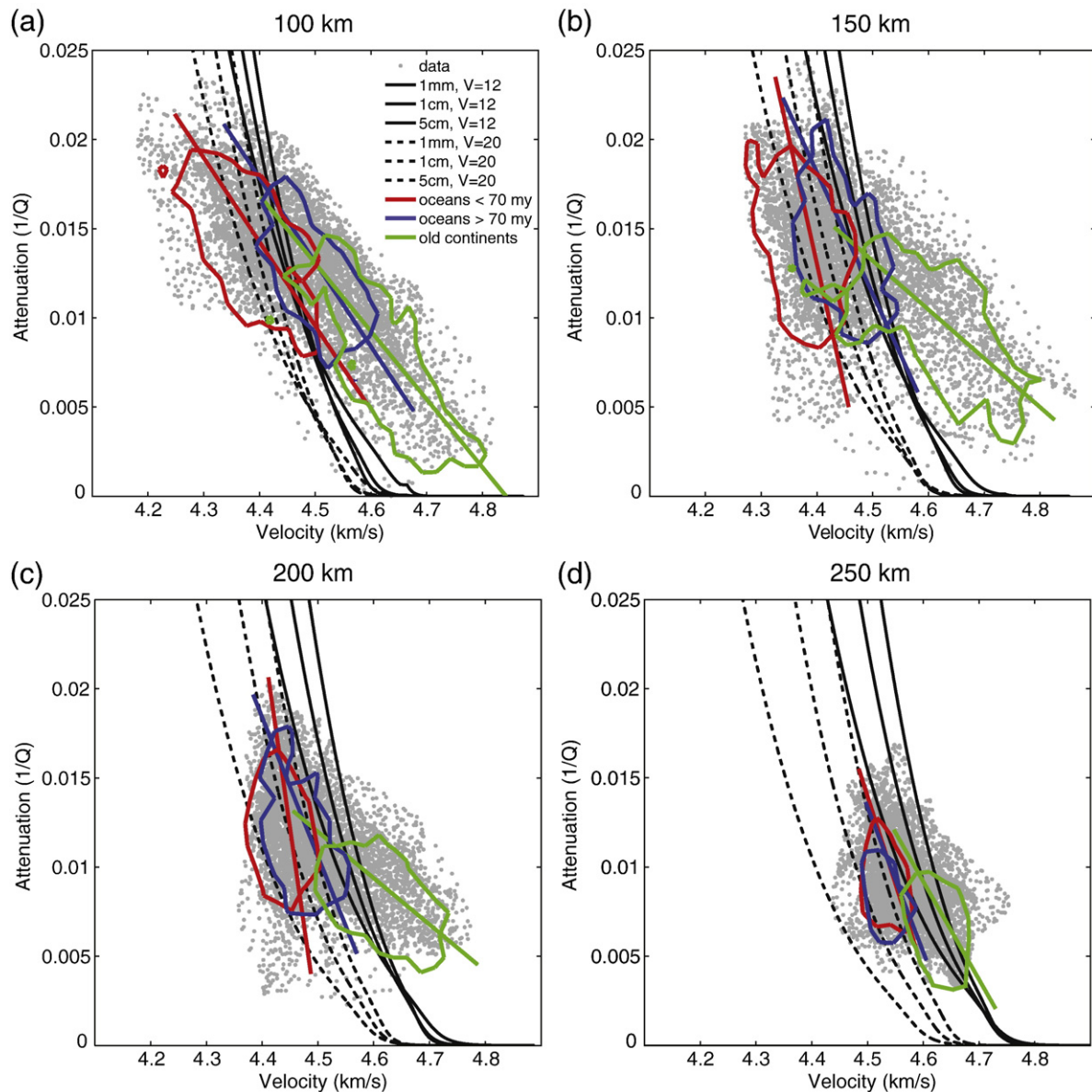


Fig. 6. Grey points show seismologically observed shear velocity (Voigt average from S362ANI) and attenuation (QRFSI12) models sampled at 5762 points. Colored contours enclose 75% of points from oceanic regions of age <70 Myr and >70 Myr and from old-continental regions. Best-fitting lines through the three groups are also shown. Black lines show the predicted relationship between shear velocity and attenuation using the model of Faul and Jackson (2005) for two activation volumes ($V = 12$ and 20×10^{-6} m³/mol) and three grain sizes. For predicted curves calculated with constant activation volume, grain size increases from left to right.

Table 2
Correlation coefficient between QRFS112 and S362ANI (*corr.*) and best-fitting value of dQ^{-1}/dV_S (*slope*) for oceanic and old-continental regions at four depths.

| | Old cont. | | Ocean <70 my | | Ocean >70 my | |
|--------|-----------|------------------------------|--------------|------------------------------|--------------|------------------------------|
| | 991 pts | 30 degrees of freedom | 2308 pts | 71 degrees of freedom | 1207 pts | 36 degrees of freedom |
| | Corr. | Slope | Corr. | Slope | Corr. | Slope |
| 100 km | -0.79 | -0.038 (-0.029 to -0.050) | -0.61 | -0.047 (-0.038 to -0.061) | -0.56 | -0.047 (-0.032 to -0.068) |
| 150 km | -0.60 | -0.027 (-0.017 to -0.040) | -0.32 | -0.14 (-0.092 to -0.30) | -0.35 | -0.068 (-0.042 to -0.11) |
| 200 km | -0.51 | -0.026 (-0.015 to -0.040) | -0.20 | -0.22 (-0.13 to -0.83) | -0.33 | -0.078 (-0.049 to -0.13) |
| 250 km | -0.51 | -0.055 (-0.036 to -0.090) | -0.22 | -0.10 (-0.071 to -0.16) | -0.28 | -0.081 (-0.053 to -0.16) |

Unless otherwise noted, correlation coefficients are significant at >95% confidence. Those italicized are significant at >90% confidence. The 95% confidence range of slope values is listed underneath the best-fitting value.

degrees of freedom. We use 170 degrees of freedom (globally) for the statistical calculations, with a smaller number for each tectonic region in proportion to the surface area of that region.

At 100-km depth, the points from the three regions form distinct groups in velocity–attenuation space that overlap only slightly (Fig. 6a); the best-fitting lines through the three groups have very similar regression coefficients that overlap within the 95%-confidence bounds (Table 2; Fig. 7a). At 150 and 200 km (Fig. 6b–c; Fig. 7b–c), the oceanic regions exhibit considerably steeper slopes dQ^{-1}/dV_S than the old-continental region does; the different velocity–attenuation characteristics of the oceanic and continental regions are significant with 95% confidence. At 250-km depth (Figs. 6d and 7d), the best-fitting slopes for the oceanic and old-continental regions agree more closely and overlap within the 95%-confidence bounds. Interestingly, at 100 and 150 km, old oceanic regions do not extend the line defined by young oceans but rather are shifted toward higher velocity and/or higher attenuation. Points beneath old oceans are characterized by either faster velocity or higher attenuation than would be expected from the trend defined by young oceanic points. This is especially evident at 150 km and does not appear to be significant at greater depth. Perhaps this observation reflects age-dependent compositional or grain-size variations within the shallow upper mantle.

For comparison with the seismological observations, Fig. 6 shows also the predicted relationships between shear velocity and attenuation, calculated with the model of Faul and Jackson (2005). These curves indicate the expected values due only to lateral variations in temperature for dry melt-free forsterite-90 olivine. Decreasing attenuation is associated with increasing velocity, and minimal attenuation is predicted to be associated with velocities larger than 4.6–4.7 km/s at all depths. In general the shape of the curves in Fig. 6 depends little on grain size and activation volume.

There is considerable overlap between the observed and predicted velocity and attenuation values, in magnitude and in trend. At 100 km, the oceanic and old-continental regions exhibit slopes (dQ^{-1}/dV_S) that are similar to each other and slightly shallower than the predicted curves. Either the range of observed attenuation values is smaller or the range of observed velocities is larger than predicted. At 150 km, the old-continental points maintain a shallower-than-predicted slope, whereas the oceanic regions more closely match the magnitude and trend predicted by the mineral-physics model. This pattern holds true for 200-km depth. At 250 km, however, the slopes for the oceanic and continental regions agree more closely, and it is no longer true that old-continental regions deviate significantly from the predicted curves.

We have established that the results in Fig. 6 are robust with respect to how strongly the attenuation model is damped. In constructing QRFS112, the squared gradient of the attenuation perturbations is minimized, and we have found that the strength of the horizontal-smoothness constraint in particular influences the reduc-

tion of data variance as well as the magnitude of lateral attenuation variations. Stronger damping results in a smoother, weaker model that provides a slightly worse fit to the data (DED08). Concerning the patterns in Fig. 6, weaker damping results in a larger spread of attenuation values, and stronger damping constricts the attenuation variations. However, while the details will differ slightly depending on the damping, the conclusions remain the same: oceanic and old-continental regions are characterized by distinctly different dQ^{-1}/dV_S values at 150 and 200 km, and that slope agrees fairly well with the mineral-physics model at depths ≥ 150 km for oceanic regions and at 250 km for old-continental regions.

4. Discussion

Given the general consistency between the seismological and experimental results (Fig. 6), the range of temperatures implied by the seismological observations can be inferred, and it is possible to consider explanations for the origin of the different velocity–attenuation characteristics of oceanic and old-continental regions. Observed attenuation and velocity provide similar estimates of temperature beneath the oceans at 150 and 200 km, owing to their agreement with the mineral-physics results. Using $d = 1$ cm and $V = 20 \times 10^{-6}$ m³/mol, a temperature range of 1300°–1500 °C is suggested beneath young oceans ($V_S = 4.3$ – 4.5 km/s; $Q^{-1} = 0.008$ – 0.021) at 150 km; slightly higher temperatures are obtained beneath old oceans if a grain size of 5 cm is assumed: 1400°–1550 °C. This range overlaps with but is much larger than the estimate for the Pacific by Priestley and McKenzie (2006), 1380°–1420 °C away from island arcs. At 200-km depth, the two oceanic regions overlap, and the observed range of attenuation and velocity ($V_S = 4.4$ – 4.5 km/s; $Q^{-1} = 0.008$ – 0.018) is consistent with $T = 1370$ °– 1550 °C, assuming $d = 1$ cm.

Estimating temperature for the old-continental regions is more complicated because (1) attenuation cannot constrain the lowest temperatures sampled by these points, since all temperatures <950 °C are assumed to yield no attenuation with the mineral-physics model, and (2) the observed points deviate from the experimental trend at depths <250 km. At 100-km depth, the 5% of all points with the fastest velocities (4.67–4.82 km/s) require temperatures in the range 580–940 °C. The fastest velocities correspond to temperatures of 670–980 °C at 150 km (4.7–4.86 km/s) and 970°–1100 °C at 200 km (4.67–4.78 km/s). We note that at 100 km the temperatures determined for old-continental regions are colder than estimates of temperature obtained from mantle xenoliths in South Africa, Siberia, and Tanzania, which are in the range 900–1000 °C (Rudnick et al., 1998). The same statement applies at 150-km depth, where the xenoliths suggest a temperature of 1100–1200 °C and the fastest velocities indicate temperatures of 650–980 °C. If present-day thermal conditions beneath cratons are inferred from the xenolith data, then temperature alone cannot explain the observed fast velocities. Cammarano and

Romanowicz (2007) reached a similar conclusion from their inversion of long-period seismic data directly for global 3-D temperature variations. They interpreted the unreasonably cold temperatures beneath cratons as an artifact due to not accounting for the depleted composition of cratons.

We focus on Fig. 6 to discuss possible interpretations of the seismological observations, considering first the slope dQ^{-1}/dV_S that characterizes each region. For the oceanic regions, the slope changes from shallow to steep in between 100 and 150 km. Within the old-continental regions, the slope changes from shallow to steep in the depth range 200–250 km. It is clear that (1) the oceanic and old-continental regions are characterized by different values of dQ^{-1}/dV_S at 150 and 200 km, and (2) both regions undergo a change toward a steeper slope that provides better agreement with the mineral-physics model; this slope-steepening occurs in the depth range 100–150 km for the oceans and 200–250 km for old continents. If it is assumed that the model of Faul and Jackson (2005) accurately describes the effects of temperature on shear velocity and attenuation in dry melt-free Fo_{90} olivine, then the change with depth toward better agreement with the predictions could represent a change in the

physical properties of the mantle over this depth interval. In this scenario, the observed relationship of decreasing attenuation associated with increasing velocity at some depth would be controlled by lateral temperature variations, but the slope of that thermally controlled relationship could vary by region, owing to specific physical conditions (e.g., Fig. 1). For example, under this assumption, at 100 km neither the oceans nor the old continents are perfectly consistent with lateral temperature variations in dry melt-free Fo_{90} olivine, suggesting that the conditions (composition, melt, water) must be different from dry melt-free Fo_{90} olivine in all regions. At 150 and 200 km, the oceanic regions are roughly consistent with lateral temperature variations in dry melt-free Fo_{90} olivine but the continental regions are not. At 250 km, the seismologically observed velocity–attenuation relationship could be explained by lateral temperature variations in dry melt-free Fo_{90} olivine for all regions.

We recognize that the mineral-physics model may not be appropriate for the upper mantle, given the conditions of the experiments. For example, experimental grain size and pressure are too small, requiring extrapolation of both variables. Dislocation-related anelasticity may be underestimated since the synthetic olivine

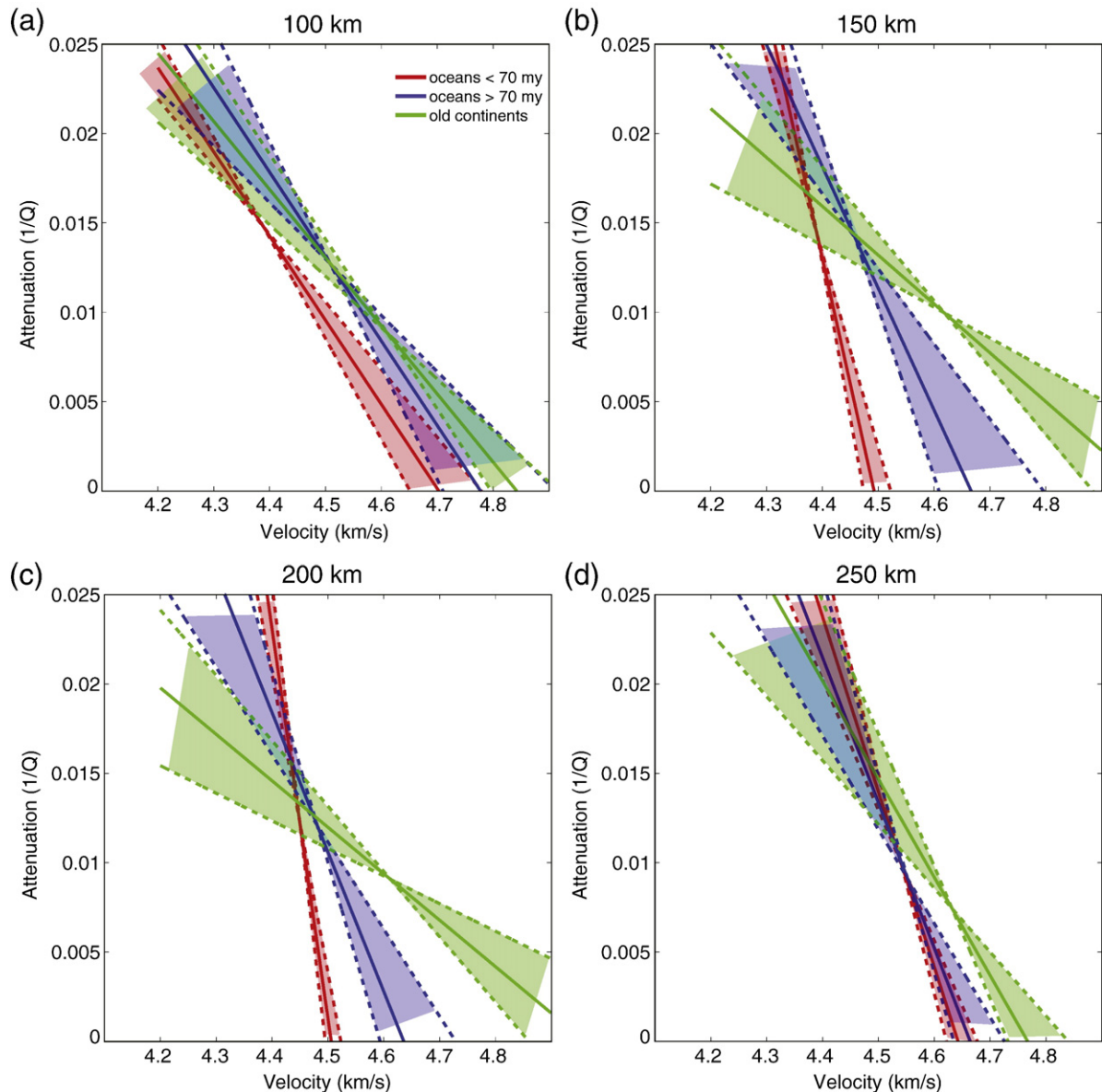


Fig. 7. Summary of 95%-confidence bounds on the best-fitting line through each tectonic region. Solid curves show the best-fitting line. Dashed lines indicate the 95%-confidence lower and upper bounds on the slope dQ^{-1}/dV_S (i.e. Table 2), and the area in between the upper and lower bounds is shaded.

samples were prepared with minimal dislocation densities so that grain-boundary processes could be studied. Also, the experiments were performed only on samples of pure olivine; effects related to the coexistence of olivine with other mineral phases (e.g., Sundberg and Cooper, 2007) and major-element compositional variations were not considered. However, even if the mineral-physics model does not accurately describe temperature-dependent attenuation and velocity in the upper mantle, the seismological observations alone still argue for differences between oceanic and continental upper mantle at 150 and 200 km that disappear at 250 km.

At this point, we can only speculate regarding mechanisms to produce the observed trends. We offer here two possible interpretations. For the first, we consider the seismological observations together with the mineral-physics model. Within old-continental mantle at depths <250 km, shear velocity is faster than the mineral-physics model predicts, and major-element compositional heterogeneity is one possible explanation. Xenoliths considered representative of the cratonic upper mantle are highly depleted in Ca, Al, and Fe and characterized by high Mg# ($100 \times \text{Mg}/(\text{Mg} + \text{Fe})$), which suggests extensive melt extraction from these rocks (e.g., Boyd, 1989; Lee et al., 2005). Lee (2003) calculated that an increase in the Mg# of garnet peridotite by 6 units leads to an increase in V_s of 0.1 km/s at STP, an indication that depleted composition could contribute to fast-velocity anomalies. Nettles (2005) combined seismic tomography and free-air gravity to estimate the effect of composition beneath cratons and found that, for an observed cratonic fast-velocity anomaly at 100-km depth, 84% of the anomaly is produced by temperature and 16% by composition. In this scenario, the faster-than-predicted continental velocities in the depth range 100–200 km in Fig. 6 represent highly depleted cratonic lithosphere. However, at depths >200 km the sub-continental mantle is not chemically distinct from the surrounding asthenosphere, allowing the seismic effects of lateral temperature variations to be similar in oceanic and continental mantle at 250 km. The shallow oceanic trend at 100 km could also have a chemical origin, reflecting melt extraction at the mid-ocean ridge. We note that Matsukage et al. (2005) have shown that at upper-mantle temperature and pressure, a fast-velocity signature of melt depletion may be weak or non-existent, which would alter our interpretation.

For the second interpretation, we consider only the seismological observations. The shift from shallower to steeper slope at ~125 km for the oceanic regions could indicate a change in the water content with depth, with a dehydrated and depleted shallow lid from which melt has been extracted overlying a hydrous asthenosphere. Although there are very few constraints on how water affects seismic properties, a steepening of the velocity–attenuation slope (Fig. 1) is expected due to increased water content (Karato, 2003; Yang et al., 2007). In this scenario, the old-continental regions transition from dry to hydrous conditions at ~225 km. Hirth et al. (2000) proposed a similar transition from dry to wet mantle based on electrical conductivity profiles. A significant change in the properties of the sub-continental mantle in the depth range 200–250 km is also consistent with recent findings in seismic anisotropy (Gung et al., 2003; Marone and Romanowicz, 2007; Nettles and Dziewonski, 2008) and xenolith composition (Lee et al., 2005).

We suggest that the depth of the transition from shallower to steeper slope in Fig. 6 may be related to the base of the lithosphere, where in this case the lithosphere must be distinguished from the material below it by factors other than temperature, such as composition or water content. The lithospheric thicknesses that are suggested by this analysis (~125 km for oceans, ~225 km for continents) are, of course, globally averaged values, and departures from these values locally are expected. We note that other seismic techniques provide better sensitivity to the lithosphere–asthenosphere boundary, for example receiver functions (e.g., Rychert et al., 2005). However, the results presented here indicate a potential usefulness of jointly interpreting attenuation and velocity models in terms of variable physical and chemical properties.

5. Conclusions

Interpretation of seismic velocity models in terms of temperature, composition, partial melt, water content, and grain size is non-unique, and we have suggested that interpreting velocity and attenuation models together helps to reduce the ambiguity. In this paper, our new global upper-mantle attenuation model is compared with global shear-wave velocity models. Attenuation and velocity are found to be anti-correlated throughout the upper mantle, particularly at shallow depths. The degree of anti-correlation is stronger than has been previously observed. Individual tectonic regions, defined by seafloor age for the oceans and by tectonic behavior of the crust during the Phanerozoic for continents, each occupy a distinct range of attenuation and velocity values at 100-km depth, and continental regions remain distinct from oceanic regions to depths of at least 200 km.

We also present the first global comparison of seismological attenuation and velocity observations with laboratory measurements of the same quantities made on fine-grained olivine and extrapolated to upper-mantle conditions. Comparison of both vertical profiles and lateral variations shows reasonably good agreement between the two sets of observations. We find that in oceanic regions, mineral-physics predictions of velocity and attenuation due to lateral temperature variations can match the seismological observations at depths >100 km, and the temperature range beneath oceans inferred from the seismic models is ~200 °C at 150- and 200-km depth. Beneath old-continental regions, the seismic observations deviate from the mineral-physics predictions at depths <250 km. We suggest that differences in the major-element composition or water content of oceanic and continental upper mantle in the depth range 150–250 km could explain the observations and may also be related to the lithosphere–asthenosphere boundary. The joint analysis of global velocity and attenuation models with experimental data shows great promise for resolving outstanding questions about the state of the Earth's interior and will be helped considerably by continued advances in experimental techniques and seismic data collection and analysis.

References

- Anderson, D.L., 1967. The anelasticity of the mantle. *Geophys. J. R. Astr. Soc.* 14, 135–164.
- Anderson, D.L., Sammis, C.G., 1970. Partial melting in the upper mantle. *Phys. Earth Planet. Inter.* 3, 41–50.
- Artemieva, I.M., Billien, M., Lévêque, J.-J., Mooney, W.D., 2004. Shear wave velocity, seismic attenuation, and thermal structure of the continental upper mantle. *Geophys. J. Int.* 157, 607–628.
- Billien, M., Lévêque, J.-J., Trampert, J., 2000. Global maps of Rayleigh wave attenuation for periods between 40 and 150 seconds. *Geophys. Res. Lett.* 27, 3619–3622.
- Boyd, F.R., 1989. Compositional distinction between oceanic and cratonic lithosphere. *Earth Planet. Sci. Lett.* 96, 15–26.
- Cammarano, F., Romanowicz, B., 2007. Insights into the nature of the transition zone from physically constrained inversion of long-period seismic data. *Proc. Nat. Acad. Sci.* doi:10.1073/pnas.0608075104.
- Dalton, C.A., Ekström, G., 2006. Global models of surface-wave attenuation. *J. Geophys. Res.* 111. doi:10.1029/2005JB003997.
- Dalton, C.A., Ekström, G., Dziewonski, A.M., 2008. The global attenuation structure of the upper mantle. *J. Geophys. Res.* 113. doi:10.1029/2007JB005429.
- Duffy, T.S., Anderson, D.L., 1989. Seismic velocities in mantle minerals and the mineralogy of the upper mantle. *J. Geophys. Res.* 94, 1895–1912.
- Dunn, R.A., Forsyth, D.W., 2003. Imaging the transition between the region of mantle melt generation and the crustal magma chamber beneath the southern East Pacific Rise with short-period Love waves. *J. Geophys. Res.* 108. doi:10.1029/2002JB002217.
- Durek, J.J., Ekström, G., 1996. A radial model of anelasticity consistent with long-period surface-wave attenuation. *Bull. Seismol. Soc. Am.* 86, 144–158.
- Ekström, G., Dziewonski, A.M., 1998. The unique anisotropy of the Pacific upper mantle. *Nature.* 394, 168–172.
- Evans, R.L., Tarits, P., Chave, A.D., White, A., Heinson, G., Filloux, J.H., Toh, H., Seama, N., Utada, H., Booker, J.R., Unsworth, M.J., 1999. Asymmetric electrical structure in the mantle beneath the East Pacific Rise at 17°S. *Science.* 286, 752–756.
- Evans, R.L., Hirth, G., Baba, K., Forsyth, D., Chave, A., Mackie, R., 2005. Geophysical evidence from the MELT area for compositional controls on oceanic plates. *Nature.* 437, 249–252.
- Faul, U.H., Jackson, I., 2005. The seismological signature of temperature and grain size variations in the upper mantle. *Earth Planet. Sci. Lett.* 234, 119–134.
- Faul, U.H., Fitz Gerald, J.D., Jackson, I., 2004. Shear wave attenuation and dispersion in melt-bearing olivine polycrystals: 2. Microstructural interpretation and seismological implications. *J. Geophys. Res.* 109. doi:10.1029/2003JB002407.

- Forsyth, D.W., 1992. Geophysical constraints on mantle flow and melt generation beneath mid-ocean ridges. *Mantle flow and melt generation at mid-ocean ridges*. AGU Geophysical Monograph, 71, 1–65.
- Gaherty, J.B., Jordan, T.H., Gee, L.S., 1996. Seismic structure of the upper mantle in a central Pacific corridor. *J. Geophys. Res.* 101, 22,291–22,309.
- Gaherty, J.B., Kato, M., Jordan, T.H., 1999. Seismological structure of the upper mantle: a regional comparison of seismic layering. *Phys. Earth Planet. Inter.* 110, 21–41.
- Goes, S., Govers, R., Vacher, P., 2000. Shallow mantle temperatures under Europe from *P* and *S* wave tomography. *J. Geophys. Res.* 105, 11,153–11,169.
- Gribb, T.T., Cooper, R.F., 1998. Low-frequency shear attenuation in polycrystalline olivine: grain boundary diffusion and the physical significance of the Andrade model for viscoelastic rheology. *J. Geophys. Res.* 103, 27,267–27,279.
- Gung, Y.C., Romanowicz, B., 2004. Q tomography of the upper mantle using three-component long-period waveforms. *Geophys. J. Int.* 157, 813–830.
- Gung, Y.C., Panning, M., Romanowicz, B., 2003. Global anisotropy and the thickness of continents. *Nature* 422, 707–711.
- Hammond, W.C., Humphreys, E.D., 2000a. Upper mantle seismic wave velocity: effects of realistic partial melt geometries. *J. Geophys. Res.* 105, 10,975–10,986.
- Hammond, W.C., Humphreys, E.D., 2000b. Upper mantle seismic wave attenuation: effects of realistic partial melt distribution. *J. Geophys. Res.* 105, 10,987–10,999.
- Harmon, N., Forsyth, D.W., Weeraratne, D., 2009. Thickening of young Pacific lithosphere from high-resolution Rayleigh wave tomography: a test of the conductive cooling model. *Earth Planet. Sci. Lett.* 278, 96–106.
- Hirth, G., Kohlstedt, D.L., 1996. Water in the oceanic mantle: implications for rheology, melt extraction, and the evolution of the lithosphere. *Earth Planet. Sci. Lett.* 144, 93–108.
- Hirth, G., Evans, R.L., Chave, A.D., 2000. Comparison of continental and oceanic upper mantle electrical conductivity: is the Archean lithosphere dry? *Geochem. Geophys. Geosyst.* 1 2000GC000048.
- Humler, E., Thiriot, J.L., Montagner, J.P., 1993. Global correlations of mid-ocean-ridge basalt chemistry with seismic tomographic images. *Nature*. 364, 225–228.
- Ishii, M., Tromp, J., 1999. Normal-mode and free-air gravity constraints on lateral variations in velocity and density of Earth's mantle. *Science*. 285, 1231–1236.
- Jackson, I., Fitz Gerald, J.D., Faul, U.H., Tan, B.H., 2002. Grain-size-sensitive seismic wave attenuation in polycrystalline olivine. *J. Geophys. Res.* 107. doi:10.1029/2001JB001225.
- Jackson, I., Faul, U.H., Fitz Gerald, J.D., Tan, B.H., 2004. Shear wave attenuation and dispersion in melt-bearing olivine polycrystals: 1. Specimen fabrication and mechanical testing. *J. Geophys. Res.* 109. doi:10.1029/2003JB002406.
- James, J.E., Boyd, F.R., Schutt, D., Bell, D.R., Carlson, R.W., 2004. Xenolith constraints on seismic velocities in the upper mantle beneath southern Africa. *Geochem. Geophys. Geosyst.* 5, Q01002.
- Jordan, T.H., 1979. Mineralogies, densities, and seismic velocities of garnet lherzolites and their geophysical implications. *The Mantle Sample: Inclusions in Kimberlites and Other Volcanics*, pp. 1–14.
- Jordan, T.H., 1981. Global tectonic regionalization for seismological data analysis. *Bull. Seismol. Soc. Am.* 71, 1131–1141.
- Karato, S., 2003. Mapping water content in the upper mantle. *Inside the Subduction Factory*. AGU Geophys. Monogr. 138, 135–152.
- Karato, S., Jung, H., 1998. Water, partial melting and the origin of the seismic low velocity and high attenuation zone in the upper mantle. *Earth Planet. Sci. Lett.* 157, 193–207.
- Kustowski, B., Ekström, G., Dziewonski, A.M., 2008. Anisotropic shear-wave velocity structure of the Earth's mantle: a global model. *J. Geophys. Res.* 113. doi:10.1029/2007JB005169.
- Lawrence, J.F., Shearer, P.M., Masters, G., 2006. Mapping attenuation beneath North America using waveform cross-correlation and cluster analysis. *Geophys. Res. Lett.* 33. doi:10.1029/2006GL025813.
- Lee, C.-T.A., 2003. Compositional variation of density and seismic velocities in natural peridotites at STP conditions: implications for seismic imaging of compositional heterogeneities in the upper mantle. *J. Geophys. Res.* 108. doi:10.1029/2003JB002413.
- Lee, C.-T.A., Lenardic, A., Cooper, C.M., Niu, F., Levander, A., 2005. The role of chemical boundary layers in regulating the thickness of continental and oceanic thermal boundary layers. *Earth Planet. Sci. Lett.* 230, 379–395.
- Liu, H.P., Anderson, D.L., Kanamori, H., 1976. Velocity dispersion due to anelasticity; implications for seismology and mantle composition. *Geophys. J. R. Astr. Soc.* 47, 41–58.
- Lizarralde, D., Chave, A., Hirth, G., Schultz, A., 1995. Northeastern Pacific mantle conductivity profile from long-period magnetotelluric sounding using Hawaii-to-California submarine cable data. *J. Geophys. Res.* 100, 17,837–17,854.
- Marone, F., Romanowicz, B., 2007. The depth distribution of azimuthal anisotropy in the continental upper mantle. *Nature*. 447, 198–201.
- Matsukage, K.N., Nishihara, Y., Karato, S., 2005. Seismological signature of chemical differentiation of Earth's upper mantle. *J. Geophys. Res.* 110. doi:10.1029/2004JB003504.
- Mierdel, K., Keppler, H., Smyth, J.R., Langenhorst, F., 2007. Water solubility in aluminous orthopyroxene and the origin of Earth's asthenosphere. *Science*. 315, 364–368.
- Nettles, M.K., 2005. Anisotropic Velocity Structure of the Mantle Beneath North America. Ph.D. Thesis. Harvard University.
- Nettles, M., Dziewonski, A.M., 2008. Radially anisotropic shear velocity structure of the upper mantle globally and beneath North America. *J. Geophys. Res.* 113. doi:10.1029/2006JB004819.
- Nishimura, C.E., Forsyth, D.W., 1989. The anisotropic structure of the upper mantle in the Pacific. *Geophys. J. Int.* 96, 203–229.
- Panning, M.P., Romanowicz, B., 2006. A three-dimensional radially anisotropic model of shear velocity in the whole mantle. *Geophys. J. Int.* 167. doi:10.1111/j.1365-246X.2006.03100.x.
- Priestley, K., McKenzie, D., 2006. The thermal structure of the lithosphere from shear wave velocities. *Earth Planet. Sci. Lett.* 244, 285–301.
- Reid, F.J.L., Woodhouse, J.H., van Heijst, H.J., 2001. Upper mantle attenuation and velocity structure from measurements of differential *S* phases. *Geophys. J. Int.* 145, 615–630.
- Ritsema, J., van Heijst, H.-J., Woodhouse, J.H., 1999. Complex shear wave velocity structure imaged beneath Africa and Iceland. *Science*. 286, 1925–1928.
- Ritzwoller, M.H., Shapiro, N.M., Zhong, S.-J., 2004. Cooling history for the Pacific lithosphere. *Earth Planet. Sci. Lett.* 226, 69–84.
- Romanowicz, B., 1990. The upper mantle degree 2: constraints and inferences from global mantle wave attenuation measurements. *J. Geophys. Res.* 95, 11,051–11,071.
- Romanowicz, B., 1994. On the measurement of anelastic attenuation using amplitudes of low-frequency surface waves. *Phys. Earth Planet. Inter.* 84, 179–191.
- Romanowicz, B., 1995. A global tomographic model of shear attenuation in the upper mantle. *J. Geophys. Res.* 100, 12,375–12,394.
- Romanowicz, B., Gung, Y., 2002. Superplumes from the core-mantle boundary to the lithosphere: implications for heat flux. *Science*. 296, 513–516.
- Roth, E.G., Wiens, D.A., Zhao, D., 2000. An empirical relationship between seismic attenuation and velocity anomalies in the upper mantle. *Geophys. Res. Lett.* 27, 601–604.
- Rudnick, R.L., McDonough, W.F., O'Connell, R.J., 1998. Thermal structure, thickness and composition of continental lithosphere. *Chem. Geol.* 145, 395–411.
- Rychert, C.A., Fischer, K.M., Rondenay, S., 2005. A sharp lithosphere–asthenosphere boundary imaged beneath eastern North America. *Nature*. 436, 542–545.
- Sato, H., Sacks, I.S., Takahashi, E., Scarfe, C.M., 1988. Geotherms in the Pacific Ocean from laboratory and seismic attenuation studies. *Nature*. 336, 154–156.
- Schutt, D.L., Leshner, C.E., 2006. Effects of melt depletion on the density and seismic velocity of garnet and spinel lherzolite. *J. Geophys. Res.* 111. doi:10.1029/2003JB002950.
- Selby, N.D., Woodhouse, J.H., 2000. Controls on Rayleigh wave amplitudes: attenuation and focusing. *Geophys. J. Int.* 142, 933–940.
- Selby, N.D., Woodhouse, J.H., 2002. The Q structure of the upper mantle: constraints from Rayleigh wave amplitudes. *J. Geophys. Res.* 107. doi:10.1029/2001JB000257.
- Shapiro, N.M., Ritzwoller, M.H., 2004. Thermodynamic constraints on seismic inversions. *Geophys. J. Int.* 157. doi:10.1111/j.1365-246X.2004.02254.x.
- Sipkin, S.A., Jordan, T.H., 1979. Frequency dependence of Q_{Scs} . *Bull. Seismol. Soc. Am.* 69, 1055–1079.
- Stein, C.A., Stein, S., 1992. A model for the global variation in oceanic depth and heat flow with lithospheric age. *Nature*. 359, 123–129.
- Stixrude, L., Lithgow-Bertelloni, C., 2005. Mineralogy and elasticity of the oceanic upper mantle: origin of the low-velocity zone. *J. Geophys. Res.* 110. doi:10.1029/2004JB002965.
- Stixrude, L., Lithgow-Bertelloni, C., 2007. Influence of phase transformations on lateral heterogeneity and dynamics in Earth's mantle. *Earth Planet. Sci. Lett.* 263, 45–55.
- Su, W.-J., Dziewonski, A.M., 1997. Simultaneous inversion for 3-D variations in shear and bulk velocity in the mantle. *Phys. Earth Planet. Inter.* 100, 135–156.
- Sundberg, M., Cooper, R.F., 2007. Shear attenuation and dispersion in harzburgite. *EOS Trans. AGU* 88, MR13C–1408.
- Tan, B.H., Jackson, I., Fitz Gerald, J.D., 2001. High-temperature viscoelasticity of fine-grained polycrystalline olivine. *Phys. Chem. Miner.* 28, 641–664.
- Trampert, J., Deschamps, F., Resovsky, J., Yuen, D., 2004. Probabilistic tomography maps chemical heterogeneities throughout the lower mantle. *Science*. 306, 853–856.
- Turcotte, D.L., Schubert, G., 1982. *Geodynamics: Applications of Continuum Physics to Geological Problems*. John Wiley and Sons, Inc., New York.
- Warren, L.M., Shearer, P.M., 2002. Mapping lateral variations in upper mantle attenuation by stacking *P* and *PP* spectra. *J. Geophys. Res.* 107. doi:10.1029/2001JB001195.
- Yang, Y., Forsyth, D.W., Weeraratne, D.S., 2007. Seismic attenuation near the East Pacific Rise and the origin of the low-velocity zone. *Earth Planet. Sci. Lett.* 258, 260–268.